Chaotic transport by Rossby waves in shear flow

Diego del-Castillo-Negrete and P. J. Morrison
Department of Physics and Institute for Fusion Studies, The University of Texas at Austin, Austin, Texas 78712

(Received 1 May 1992; accepted 7 October 1992)

Transport and mixing properties of Rossby waves in shear flow are studied using tools from Hamiltonian chaos theory. The destruction of barriers to transport is studied analytically, by using the resonance overlap criterion and the concept of separatrix reconnection, and numerically by using Poincaré sections. Attention is restricted to the case of symmetric velocity profiles with a single maximum; the Bickley jet with velocity profile sech^2 is considered in detail. Motivated by linear stability analysis and experimental results, a simple Hamiltonian model is proposed to study transport by waves in these shear flows. Chaotic transport, both for the general case and for the sech^2 profile, is investigated. The resonance overlap criterion and the concept of separatrix reconnection are used to obtain an estimate for the destruction of barriers to transport and the notion of *banded* chaos is introduced to characterize the transport that typically occurs in symmetric shear flows. Comparison between the analytical estimates for barrier destruction and the numerical results is given. The role of potential vorticity conservation in chaotic transport is discussed. An area preserving map, termed *standard nontwist* map, is obtained from the Hamiltonian model. It is shown that the map reproduces the transport properties and the separatrix reconnection observed in the Hamiltonian model. The conclusions reached are used to explain experimental results on transport and mixing by Rossby waves in rotating fluids.

I. INTRODUCTION

The goal of this work is to use some ideas from Hamiltonian chaos theory to study transport properties of Rossby waves in shear flow. Attention is restricted to the case of symmetric shear flows of the form of zonal flows; in particular, the Bickley jet[1] with the velocity profile $\propto \mathrm{sech}^2 y$ is considered in detail.

Zonal shear flows occur naturally in both the oceans and the atmosphere; two well-known examples are the Gulf stream and the polar night jet above Antarctica. Barotropic perturbations of these zonal flows produce Rossby waves[2] that have a crucial influence on transport and mixing, and an understanding of these transport properties is a major problem of geophysical fluid dynamics. Needless to say, the real situation in the oceans and atmosphere is much more complicated than the simple model we are to present. However, as in many cases, a simplification of the real situation lends insight and gives rise to useful qualitative ideas.

Being two dimensional and incompressible the flows we consider can be described by a streamfunction ψ. Hence, the Lagrangian trajectory $[x(t),y(t)]$ of a fluid particle or of an advected passive scalar is described by the equations

$$\frac{dx}{dt}=-\frac{\partial\psi}{\partial y}, \qquad \frac{dy}{dt}=\frac{\partial\psi}{\partial x}. \tag{1}$$

These equations are Hamilton's equations with the streamfunction identified as the Hamiltonian and the physical space (x,y) identified as the phase space (q,p). The form of Eqs. (1) makes it possible to study transport in two-dimensional incompressible hydrodynamics using the well-developed methods of Hamiltonian dynamics (see, for example, Ref. 3). It is well known that all time-independent one-degree-of-freedom Hamiltonian systems are integrable. Therefore, in a fluid with a time-independent streamfunction all fluid particles move in a nonchaotic or integrable way, following the contours of constant ψ. When time dependence is added the Hamiltonian system is usually not integrable, and so chaotic motion is likely to appear, giving rise to what is referred to as chaotic advection or "Lagrangian turbulence."[4–7] By chaotic transport we mean the transport that occurs when the fluid velocity field is not chaotic, but the fluid particle trajectories exhibit chaotic behavior. Regions of high mixing and transport in the fluid are identified with the chaotic regions of the associated Hamiltonian system, whereas barriers to transport are identified with integrable (nonchaotic) trajectories.

In Sec. II we review known results on propagation of Rossby waves in shear flows and consider the Bickley jet sech^2 velocity profile. Motivated by linear stability analysis, we propose a simple model for the streamfunction (Hamiltonian). Section III contains a discussion of chaotic transport by waves in a general symmetric shear flow. In Sec. III A we study the phase space of a general Hamiltonian that models waves in a symmetric shear flow. We show that, depending on the parameters, the phase space portrait can be of two different types and that the change from one type to the other is due to separatrix reconnection. Using the Hamiltonian function, a threshold for the reconnection is obtained. In Sec. III B we study the barriers to transport in the system using the resonance overlap criterion,[8,9] together with the criterion for separatrix reconnection. The

 0899-8213/93/040948-18$06.00

term *banded* chaos is introduced to account for the chaos that typically occurs in bands in the phase space. In Sec. III C the role of potential vorticity conservation is discussed. In the last part of Sec. III, an area preserving map that describes chaotic transport by waves in a general symmetric shear flow is obtained from the Hamiltonian system. It is shown that the map violates the so-called twist condition,[3] and that it has a very rich structure exhibiting both stochasticity and separatrix reconnection. In Sec. IV we apply the previous results to the special case of the sech^2 velocity profile. A comparison is made between the analytical estimates of the thresholds for barrier destruction and the numerically determined thresholds. In Sec. V the model is used to qualitatively explain experimental results of Sommeria *et al.*[10,11] concerning transport and mixing by Rossby waves in zonal flows in rotating fluids. Comparison of our model with previously proposed models[12,13] is made. In Sec. VI we summarize and conclude.

II. A MODEL FOR THE STREAMFUNCTION

In order to study chaotic transport the streamfunction of the system is needed. In principle, one should get this function by solving the Navier–Stokes equations with the appropriate boundary conditions. However, solutions of nonlinear fluid equations are difficult to obtain and so one has to resort to simplified approaches. One such approach is to use arguments based on linearization of the corresponding fluid equations. Within its limitations, linear theory is useful in that it sometimes gives simple ideas upon which a physically meaningful model for the stream can be constructed. On the other hand, experimental results can also be used to build a model. The goal in the present section is to obtain a simple model for the streamfunction that represents the propagation of Rossby waves in a shear flow, a model that is based on linear stability analysis[14,15] and experimental results.[10,11]

In the study of Rossby waves one considers wave motion in a two-dimensional, incompressible, inviscid, rotating shallow water system, where, in accordance with the beta plane approximation,[2] the Coriolis force is assumed to depend linearly on one coordinate. A right-handed Cartesian coordinate system with z pointing in the direction of rotation and y in the direction of the Coriolis force gradient is adopted. That is, y points in the "northward" direction and x is a periodic coordinate in the "eastward" direction. In these coordinates an equilibrium shear or zonal flow has the form

$$\mathbf{v}=u_0(y)\hat{x}. \tag{2}$$

Upon introducing the streamfunction,

$$\mathbf{v}=\hat{z}\times\nabla\psi, \tag{3}$$

the velocity field becomes

$$u_0=-\frac{\partial\psi_0}{\partial y}. \tag{4}$$

Here u_0 is assumed to be a symmetric function of y and so ψ_0 is antisymmetric. In the beta plane approximation the potential vorticity is given by

$$q=\nabla^2\psi+\beta y, \tag{5}$$

where the parameter β is related to the gradient of the Coriolis force and the basic dynamics of the system is governed by the conservation of potential vorticity:[2]

$$\frac{\partial q}{\partial t}+(\mathbf{v}\cdot\nabla)q=0. \tag{6}$$

Let ψ_1 be a small perturbation of the zonal flow,

$$\psi=\psi_0+\psi_1, \tag{7}$$

and write

$$\psi_1=\phi(y)e^{ik(x-ct)}. \tag{8}$$

Upon substituting (7) into (6) and linearizing, it is seen that $\phi(y)$ is a solution of the Rayleigh–Kuo equation,

$$(u_0-c)\left(\frac{d^2\phi}{dy^2}-k^2\phi\right)+(\beta-u_0'')\phi=0, \tag{9}$$

with the appropriate boundary condition. Because u_0 is symmetric the eigenfunctions ϕ have definite parity. Only eigenfunctions that produce symmetric perturbations of the zonal flow are considered because in the parameter regime of interest (dimensionless β near the marginal value of $\frac{2}{3}$) the antisymmetric modes are stable.[15] Throughout the present work all variables are dimensionless, the velocity scale U is defined as the maximum zonal flow velocity, and the length scale L measures the horizontal variation of the zonal flow. Hence, the dimensional variables are given by Ly, Uu, k/L, $(U/L^2)\beta$, etc. According to Eqs. (7) and (8), a general streamfunction that describes Rossby waves superimposed on an equilibrium zonal flow is given by

$$\psi=\psi_0+\sum_j\phi_j e^{ik_j(x-c_j t)}, \tag{10}$$

where ψ_0 is antisymmetric and the ϕ_j are symmetric eigensolutions of Eq. (9).

A critical layer of a zonal flow appears where the velocity c of a propagating wave matches the velocity u_0 of the zonal flow. One of the difficulties encountered in trying to solve Eq. (9) for a general profile is that the equation becomes singular at these critical layers. One way to approach this problem is to consider the effects of viscosity and/or nonlinearity in a critical layer, and then match the solutions inside and outside the layer. There is, however, the possibility of getting regular neutral wave [$\mathrm{Im}(c)=0$] solutions of the Rayleigh–Kuo equation if it occurs that $(\beta-u_0'')/(u_0-c)$ remains finite when $c=u_0$. Kuo[14] has shown that the condition for the existence of such solutions is that the gradient of potential vorticity vanish at some point y^*,

$$\beta-\frac{d^2u_0}{dy^2}(y^*)=0, \tag{11}$$

where

$$c=u_0(y^*). \tag{12}$$

These waves are marginal, that is, they represent a stability boundary in parameter space between unstable [$\mathrm{Im}(c)>0$] and asymptotically stable [$\mathrm{Im}(c)<0$] waves.

Therefore a zonal flow satisfying

$$\frac{d^2u_0}{dy^2}-\beta=a(u_0-c_1)(u_0-c_2), \tag{13}$$

where a is some constant and $u_{0\,\min} < c_{1,2} < u_{0\,\max}$, will be capable of supporting two neutral waves. A solution to this equation is given by

$$u_0=\mathrm{sech}^2 y, \tag{14}$$

with $a=-6$. This velocity profile is known as the *Bickley jet.*[1] By construction, the potential vorticity of this profile is flat (i.e., $\partial q/\partial y=0$) at points $\pm y_1^*$ and $\pm y_2^*$; it satisfies (11) and hence admits the two neutral waves. The phase velocities of these waves are given by[15]

$$c_{1,2}=\tfrac{1}{3}(1\pm\Delta), \tag{15}$$

$$\Delta=\sqrt{1-\tfrac{3}{2}\beta}, \quad \beta\in(0,\tfrac{2}{3}), \tag{16}$$

and the positions of the critical layers are given by

$$y_{1,2}^*=\mathrm{sech}^{-1}\sqrt{\frac{1\pm\Delta}{3}}. \tag{17}$$

For $\beta=\frac{2}{3}$ the velocities of the two waves merge to the value $\frac{1}{3}$ and the critical points coincide at $y^*=\mathrm{sech}^{-1}(1/\sqrt{3})$. When β tends to zero the velocity of the fast mode approaches the maximum value of $\frac{2}{3}$ and its critical points tend to $\mathrm{sech}^{-1}(\sqrt{2/3})$, whereas the velocity of the slow mode goes to zero and its critical points tend to $\pm\infty$. For the velocity profile (14) the symmetric neutral solutions to the Rayleigh–Kuo equation are given by[15]

$$\phi(y)=\mathrm{sech}^2 y, \tag{18}$$

$$k_{1,2}^2=6c_{1,2}. \tag{19}$$

Between these marginally stable modes exists a band of unstable or growing modes with phase velocities and wave numbers in the range $c_1<\mathrm{Re}(c)<c_2$ and $k_1<k<k_2$, respectively, for $0<\beta<\frac{2}{3}$. Since these unstable modes grow exponentially, the linear calculation becomes invalid after some time. The system has finite energy and the growing process eventually stops because of nonlinear saturation effects, wave–zonal flow interaction, and perhaps dissipation. Because the system is assumed periodic in the x direction, the only allowed wave numbers satisfy the wavelength quantization condition $m\lambda=D$, where λ is the wavelength, m an integer, and D the spatial period. Usually, in linear theory there is a single mode with the maximum growth rate; however, in the case we are considering, due to the wavelength quantization two modes can have comparable growth rates. We will say that a system is in its marginal state if the only modes that satisfy the quantization condition are the neutral modes. For an arbitrary change in the value of β the system is no longer at marginality. However, as the unstable modes grow the wave–zonal flow interaction can change the maximum velocity and width of the jet, so that the system relaxes to the marginal stable state and the growing process stops. In general, the barotropic instability tends to reduce the maximum velocity U and to increase the width L of the jet.[2] This change of scales increases the value of the dimensionless β coefficient and thus by the Rayleigh–Kuo stability criterion increases the stability of the jet. Eventually the jet will adjust to the marginally stable state, where no growing mode can be excited. The relaxation of an eastward jet to marginal stability was observed experimentally by Sommeria *et al.*[10,11] They measured the radial profile of the azimuthal average of the azimuthal component of the velocity field and observed that to a good approximation the jet was in its marginally stable state. Also, they observed that the scaling of the jet's maximum velocity with system parameters approximates well the scaling expected from marginal stability. Finally, the range of wavelengths observed in the experiment agree qualitatively with the predictions obtained from marginal stability arguments.[7,11]

Motivated by the preceding linear stability results and the experimental evidence of the relaxation to marginal stability, we propose as a model for the streamfunction a superposition of the zonal flow and the two neutral modes that exist at marginality,

$$\psi=-\tanh y+\mathrm{sech}^2 y\sum_{i=1}^{2}\varepsilon_i\cos k_i(x-c_i t), \tag{20}$$

where the c_i and k_i are given by Eqs. (15) and (19). This model for the streamfunction was originally proposed by the authors in Ref. 7. Although in a real situation (e.g., the Sommeria *et al.* experiment[10,11]) nonlinear effects may give rise to a more complicated streamfunction, the above simplified model will capture many of the transport properties of the system. In general, the study of the mixing and transport properties of fluids by employing simple low degrees of freedom Hamiltonian systems has proven fruitful (see, for example, Refs. 4–7, 12, 13, 16–19, and 21).

III. CHAOTIC TRANSPORT IN A GENERAL SYMMETRIC SHEAR FLOW

In the present section we discuss some general results on chaotic transport that depend only upon both the zonal flow velocity and perturbation eigenfunctions being symmetric and having a single maximum.

A. Phase space structure

Consistent with Eq. (10) is the following general Hamiltonian that models the motion of a passive scalar in a symmetric shear flow with Rossby waves:

$$H=H_0(y)+\sum_i\varepsilon_i\phi_i(y)\cos k_i(x-c_i t), \tag{21}$$

where in this section H_0 is an arbitrary antisymmetric function with a single inflection point and ϕ_i is an arbitrary symmetric function with a single maximum. This Hamiltonian has the standard structure, possessing an integrable

part H_0, that represents the zonal flow, and a nonintegrable small perturbation that represents the waves.

In order to characterize the phase space of this Hamiltonian in a simple way, only a single mode is considered. After canonically transforming to a frame comoving with the wave, the single-mode Hamiltonian H_i becomes

$$H_i=H_0(y)+\varepsilon_i\phi_i(y)\cos(k_ix)+c_iy. \tag{22}$$

The fixed (stagnation) points $(\tilde{x},\tilde{y})$ are solutions of the equations

$$\dot{x}=-\frac{dH_0}{dy}-\varepsilon_i\frac{d\phi_i}{dy}\cos(k_ix)-c_i=0, \tag{23}$$

$$\dot{y}=-\varepsilon_ik_i\phi_i\sin k_ix=0. \tag{24}$$

In the case of interest $\phi_i>0$ everywhere; therefore, from Eq. (24),

$$\tilde{x}_i=\frac{n\pi}{k_i}, \quad n=0,1,..., \tag{25}$$

and Eq. (23) becomes

$$\frac{dH_0}{dy}+(-1)^n\varepsilon_i\frac{d\phi_i}{dy}+c_i=0. \tag{26}$$

In general, this is a transcendental equation for $\tilde{y}$ and cannot be solved explicitly. However, for ε_i small, an approximate solution to first order in epsilon is given by

$$\tilde{y}_i\approx\tilde{y}_i^{(0)}+\varepsilon_i\tilde{y}_i^{(1)}. \tag{27}$$

Expanding H_0 and ϕ_i in Taylor series near $\tilde{y}_i^{(0)}$ yields

$$\tilde{y}_i=(-1)^n(y_i^*+\varepsilon_iA_i), \tag{28}$$

where

$$A_i=-\frac{(d\phi_i/dy)_{y_i^*}}{(d^2H_0/dy^2)_{y_i^*}}, \tag{29}$$

and y_i^* is the location of the critical layer [cf. Eq. (12)]. In a symmetric zonal flow d^2H_0/dy^2 is positive (negative) for y positive (negative), while on the other hand, for symmetric perturbations $d\phi_i/dy$ is negative (positive) for y positive (negative). Therefore A_i is always positive, and the fixed points are shifted a distance of order ε_i with respect to the critical layer.

The stability of a given fixed point is determined by linearizing the equations of motion. For Hamiltonian systems, if the eigenvalues of the matrix representing the linearized equations are real then the fixed point is hyperbolic (unstable), whereas if the eigenvalues are complex conjugates the fixed point is elliptic (neutrally stable). For a single degree-of-freedom Hamiltonian system the point $(\tilde{x},\tilde{y})$ is elliptic if and only if

$$\left[\left(\frac{\partial^2H}{\partial x^2}\right)\left(\frac{\partial^2H}{\partial y^2}\right)-\left(\frac{\partial^2H}{\partial x\,\partial y}\right)^2\right]_{(\tilde{x},\tilde{y})}>0. \tag{30}$$

Upon substituting Eq. (22) into this condition it is seen that to first order in epsilon the fixed point is elliptic if and only if

$$(-1)^{n+1}\frac{d^2H_0}{dy^2}(\tilde{y}_i)>0. \tag{31}$$

Note that, at this order, the stability depends only on the sign of the zonal flow vorticity.

Having found the fixed points and their stability properties, the next thing to consider is how the hyperbolic fixed points are connected. Because $d^2H_0/dy^2=0$ for $y=0$ this problem is nontrivial. As a matter of fact, the hyperbolic points can be joined in two ways: either as shown in Fig. 1(a), giving rise to an heteroclinic-type phase portrait, or as shown in Fig. 1(c), giving rise to an homoclinic-type phase portrait. The change from one portrait to the other is a global bifurcation called *separatrix reconnection*. If we denote by P and Q the hyperbolic points located above and below the $y=0$ line, respectively, then at the threshold for reconnection, which corresponds to the state shown in Fig. 1(b), $H_i(P)=H_i(Q)$. On the other hand, because of the symmetry properites of $H_0(y)$ and $\phi(y)$, it is always true that $H_i(P)=-H_i(Q)$. Therefore, the threshold for reconnection reduces to $H_i(P)=0$. Since the position of the hyperbolic point P depends on ε_i and c_i, the reconnection threshold is an implicit equation for these parameters. From a physical point of view the phase portrait will have the homoclinic structure, provided the waves have large enough amplitudes and speeds close enough to the maximum speed of the zonal flow. For small wave speeds and amplitudes the phase portrait will be of heteroclinic type.

B. Resonance overlap

It is evident that with a single mode the Hamiltonian is time independent in the comoving or wave frame and is thus integrable. However, perturbation of this integrable motion by a second mode will, in general, give rise to chaotic motion. A qualitative description of how the presence of two modes generates chaotic trajectories is provided by the Chirikov resonance overlap criterion.[8,9] Also, this criterion is useful for estimating the location and size of the chaotic regions.

For a Hamiltonian of the type (21) *resonances* y_i^* are defined as the places where the frequency of the perturbations matches the frequency of the unperturbed Hamiltonian,

$$-\frac{dH_0}{dy}(y_i^*)=c_i. \tag{32}$$

Comparison with Eq. (12) reveals that critical layers in fluid mechanics correspond exactly to resonances in the Hamiltonian model. Near a resonance the unperturbed phase space is distorted giving rise to an island chain with the width dependent upon the size of the perturbation. When two modes are present the resonances compete and chaos ensues. According to the overlap criterion, the last integrable trajectory or barrier between two resonances is destroyed when the sum of the half-widths of the two resonance "islands" (calculated independently of one another) equals the distance between the resonances; that is,

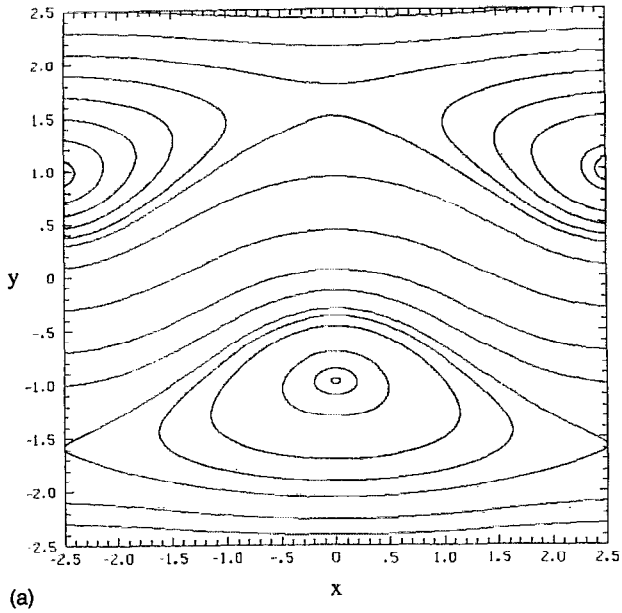

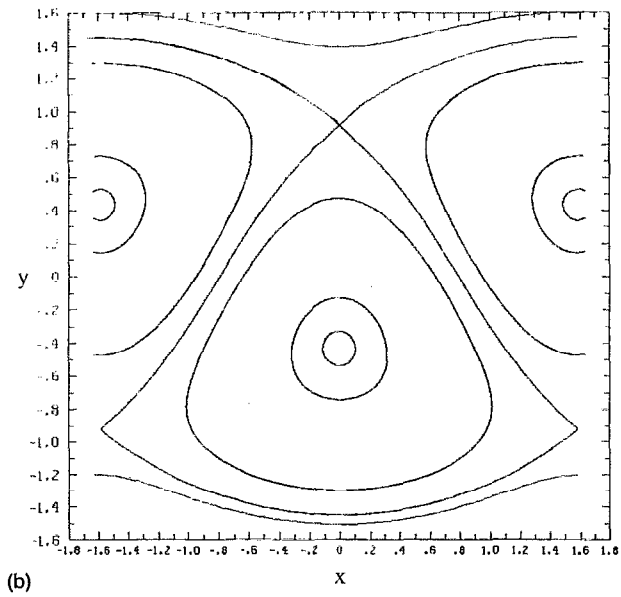

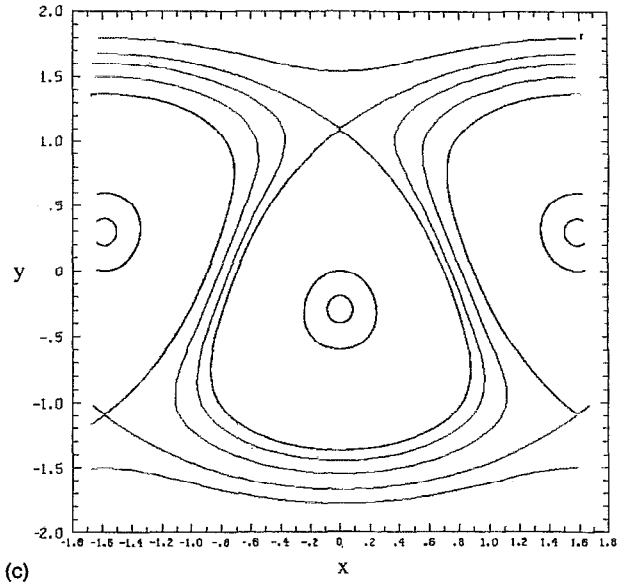

FIG. 1. Phase space of Hamiltonian (58). These are the typical phase space portraits of a general Hamiltonian representing the propagation of waves in a symmetric shear flow. As discussed in the text the type of phase structure depends on the the wave amplitudes and speeds. In (a) $\varepsilon_1=0.3$ and $\beta=0.614$ and the phase space shows a heteroclinic-type structure. In (c) the phase space shows a homoclinic-type structure with $\varepsilon_1=0.5$ and $\beta=0.052$. Case (b) shows the reconnection threshold with the predicted (see Fig. 7) parameter values $\varepsilon_1=0.275$ and $\beta=0.052$.

$$\frac{W_1}{2}+\frac{W_2}{2}=|y_2^*-y_1^*|, \tag{33}$$

where W_1, W_2 are the widths of the islands and y_i^* is the position of the ith resonance (see Fig. 2). Observe that according to the overlap criterion, barrier destruction depends not only on the strength of the perturbations (measured by W_i), but also on the frequencies of the perturbations. The latter is measured by the distance between the resonances. It is important to keep in mind that this is only a rough criterion, but it usually yields good estimates for barrier destruction. The overlap criterion is easy to apply and provides a qualitative picture of the appearance of chaos in the phase space.

To compute the width of the resonances in a simple way it is useful to make the so-called "pendulum approximation." One begins with the Hamiltonian of the i mode in its comoving frame [Eq. (22)]. Upon expanding around the resonance $y = y_i^* + p$ and using Eq. (32), the Hamiltonian becomes for small p and ε_i,

$$H_i=\frac{1}{2}p^2\left(\frac{d^2H_0}{dy^2}\right)_{y_i^*}+\varepsilon_i\phi_i(y_i^*)\cos k_i x+[H_0(y_i^*)+c_i y_i^*], \tag{34}$$

where the last term, being a constant, can be ignored. With the following definitions:

$$m_i=\left|\frac{d^2H_0}{dy^2}(y_i^*)\right|^{-1},$$
$$\gamma_i=\varepsilon_i\phi_i(y_i^*), \tag{35}$$

the Hamiltonian becomes

$$H_i=\frac{p^2}{2m_i}+\gamma_i\cos(k_i x). \tag{36}$$

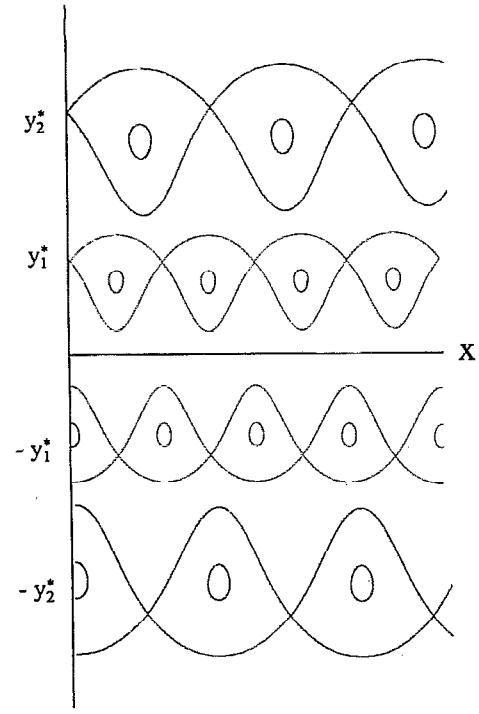

FIG. 2. Depiction of isolated resonance pairs. Banded chaos occurs when the resonance at y_1^* overlaps that at y_2^* and simultaneously because of symmetry $-y_1^*$ and $-y_2^*$ overlap. Physically this will occur for small values of ε_i, provided the difference between the wave speeds is small. The central barrier can be destroyed by the combined effect of reconnection between resonances y_1^* and $-y_1^*$ and resonance overlap between y_2^* and $-y_1^*$. From a physical point of view central barrier destruction requires large wave amplitudes and speeds close to the maximum zonal flow velocity.

In this approximation, the width of the resonance is given simply by the distance between the pendulum separatrices,

$$W_i=4\sqrt{\gamma_i m_i}, \tag{37}$$

and the overlap criterion is given by

$$\sqrt{\varepsilon_1\frac{\phi_1(y_1^*)}{|u_0'(y_1^*)|}}+\sqrt{\varepsilon_2\frac{\phi_2(y_2^*)}{|u_0'(y_2^*)|}}=\frac{1}{2}\,|y_2^*-y_1^*|. \tag{38}$$

Before proceeding to the application of the overlap criterion we discuss its limitations and possible ways for improvement. First of all, the calculation of the distances between resonances neglects the resonance interaction. In actuality, the structure of each resonance is modified by the presence of the other. In some cases the interaction between resonances is manifested as *separatrix repulsion* and it may occur that even though the approximation indicates overlap, the separatrices, in fact, do not touch.[20] A second limitation is the neglect of *higher-order resonances* that exist between the primary resonances. The overlap of these higher-order resonances may lower the stochasticity threshold. However, dominant behavior is captured by the primary resonance analysis, which is, in fact, the beginning of a more detailed calculation. A third limitation involves the role of the *stochastic layer*, a layer that exists in the vicinity of the resonances separatrices for arbitrarily small values of the mode amplitudes. Because of the stochastic layer the effective distance between resonances can be smaller than the distance between the unperturbed separatrices. Using perturbation theory, the overlap of higher-order resonances and the width of the stochastic layer can be calculated, and an improvement of the threshold for barrier destruction can be obtained.[8,9] The systematic method for calculating the effect of the higher-order resonances is called renormalization,[20] a method that consists of transforming the original Hamiltonian to a series of new Hamiltonians, each of the same form, and each of which describes successively higher-order resonances of the original system. The last limitation we discuss is the *pendulum approximation*, which we used to get a simple analytical estimate of the distances between the separatrices. This approximation neglects the asymmetric shape of the resonances that arises from nonlinearity. The approximation is good provided the terms neglected in the Taylor expansion of the Hamiltonian are small. This will occur if the values of epsilon are small and the resonances are not too close to the $y=0$ line, where the "mass" of the pendulum becomes arbitrarily large. In any case, the exact distance between the unperturbed separatrices can be obtained numerically to get a better threshold for overlap. The main advantages of the overlap criterion presented is that it is a heuristic criterion for understanding the appearance of chaos and for obtaining a simple estimate of barrier destruction. However, this and the above limitations must be borne in mind when applying Eq. (38), a task to which we now turn.

Depending on the width and relative positions of the resonances one can distinguish several types of chaotic transport in the system. The first corresponds to the case where the resonances are far enough from each other so that no overlap occurs. In this case the vicinity of the line $y=0$ will have invariant curves, and, in addition, there will be invariant curves separating y_1^* from y_2^* and $-y_1^*$ from $-y_2^*$ (see Fig. 2). Each of the resonances will have its own stochastic layer, but transport between the resonances will not occur [see, for example, Fig. 8(a)].

The next case corresponds to the situation when the resonance located at y_2^* overlaps that located at y_1^*, while both remain above the line $y=0$, and because of symmetry, $-y_2^*$ will overlap $-y_1^*$ below $y=0$. This overlap destroys the invariant curves between y_1^* and y_2^* (and simulaneously those between $-y_1^*$ and $-y_2^*$), resulting in symmetric bands of chaos separated by a band of nearly integrable trajectories spanning the central region. We refer to this case as *banded chaos*. Because the phase space is two dimensional, the invariant tori of the nearly integrable region near $y=0$ divides the phase space into two regions, precluding transport across the central region.

In the banded chaos regime there exist two different situations depending on the strength of the perturbations. For small perturbations there are finite regions of stability or "islands" around the primary elliptic fixed points [see, for example, Fig. 8(b)]. These islands of stability correspond to the regions of trapped particles in the fluid and so

we refer to this regime as *banded chaos with trapping regions*. For stronger perturbations the primary elliptic fixed points become unstable and the islands of stability are destroyed [see Fig. 8(c)]. We refer to this case as *banded chaos without trapping regions*.

The last case corresponds to the situation where the integrable trajectories in the vicinity of the $y=0$ line are destroyed. The barrier destruction in this case is more complicated and interesting than the banded chaos case, since the central barrier destruction is caused by both the overlap of resonances, producing stochasticity, and the overlap of resonances, producing separatrix reconnection. The interplay between stochasticity and reconnection in a Hamiltonian system was studied for a particular area preserving map in Ref. 22. In Sec. III D we construct an area preserving map model for studying transport by waves in a general symmetric shear flow and consider the reconnection that takes place. Detailed study of the central barrier destruction will be the subject of a future work. Here, we describe only some general features of the problem. The source of the interesting phenomena and difficulties encountered in the central barrier destruction lies in the fact that the general Hamiltonian model for waves in a symmetric shear flow (21) is *degenerate*; i.e., $d^2H_0/dy^2=0$ at $y=0$. Physically this occurs because the zonal flow velocity profile has a maximum. As we will discuss in Sec. III D this is reflected in the violation of the *twist condition* in the associated area preserving map. Degenerate Hamiltonians and nontwist maps have not been studied in detail, and most of the well-established results in Hamiltonian mechanics do not apply to them. It is precisely the degeneracy of the Hamiltonian (or the violation of the twist condition in the case of the map) that allows the possibility of separatrix reconnection in the system. As a first approximation to the central barrier destruction problem we consider simultaneously the threshold for primary resonances overlap of mode one ($+y_1^*$ and $-y_1^*$), producing reconnection, and the threshold for the overlap of primary resonances located at $+y_2^*$ and $-y_1^*$ (or equivalently $+y_1^*$ and $-y_2^*$), producing stochasticity. Evidently, in the vicinity of the reconnection threshold, the presence of the stochastic layer in the reconnecting mode can destroy the central barrier for arbitrary small values of the mode-two amplitude [see Fig. 8(d)]; therefore, the reconnection threshold gives an upper bound for the central barrier destruction threshold. However, the central barrier can also be destroyed before the reconnection process takes place by the overlapping of resonance $+y_2^*$ and $-y_1^*$ (or equivalently $+y_1^*$ and $-y_2^*$), in which case the Chirikov criterion will provide an approximate threshold. In Sec. IV, where the case of the sech^2 zonal flow is considered, it is seen that these ideas provide an upper bound for the threshold of central barrier destruction consistent with the numerical results.

From a physical point of view, banded chaos will occur for small values of epsilon if the difference between the wave speeds, that determine the resonance positions, is small. On the other hand, the central barrier will be broken provided the wave amplitudes are big enough or the wave speeds large enough. If the wave speeds have an upper bound sufficiently lower than the maximum velocity of the zonal shear flow, then the central barrier will be preserved if the wave amplitudes are small. Numerical evidence shows that reconnection of higher order islands in both the map [see Figs. 4(b) and 4(c)] and the Hamiltonian model may lead eventually to central barrier destruction, a phenomena observed also in Ref. 22. This scenario of barrier destruction due to reconnection is quite different from the "standard" scenario of usual twist maps (e.g., the standard map) and nondegenerate Hamiltonians. In what follows we consider only central barrier destruction when the primary resonances have the heteroclinic topology, the one that occurs in most cases of physical relevance in the present work. Central barrier destruction when the primary resonances have the homoclinic structure is reserved for a future publication. Finally, we note that it is possible to have central barrier destruction without having banded chaos, a situation illustrated in Fig. 8(d). For global chaos all transport barriers must be destroyed.

C. Chaotic transport and potential vorticity conservation

In this section the issue of self-consistency between potential vorticity conservation and chaotic transport is addressed. If potential vorticity is conserved then advected particles must follow the contours of constant q. Since the velocity field is assumed nonchaotic, contours of constant q evolve in a nonchaotic way; therefore, the fluid particles following these contours can not exhibit chaotic behavior. Thus we arrive at an apparent contradiction between the coexistence of chaos and potential vorticity conservation.

However, this "contradiction" does *not* exist if the potential vorticity is constant in some finite, two-dimensional spatial region. In such a region potential vorticity conservation and chaotic advection are consistent because fluid particles are able to mix chaotically while preserving their constant value of potential vorticity. For the model of Eq. (21) regions of banded chaos coincide with regions where the potential vorticity is nearly constant. This is because Kuo's theorem [Eq. (11)] requires that neutral modes exist at places where $\partial q_0/\partial y=0$. In the Hamiltonian picture the neutral modes create resonances and these are located in regions where the potential vorticity tends to be constant. If the resonances y_1^* and y_2^* (the same applies to $-y_1^*$ and $-y_2^*$) are close enough together, then the potential vorticity is nearly constant in the region between them. At the same time, the overlap criterion predicts chaotic motion in just this region. This is consistent with the observation[23] that regions of constant potential vorticity correspond to mixing regions. On the other hand, our explanation of central barrier persistance, presented in the previous section, is consistent with arguments based on the steepness of the potential vorticity gradient.[23] To see this, note that for the model we are studying, the potential vorticity gradient at $y=0$ is given by $dq_0/dy=a(U-c_1)(U-c_2)$, where U is the zonal flow maximum velocity [see Eq. (13)]. Therefore, to have a large gradient of potential vorticity c_1 and c_2 must be sufficiently below the maximum zonal flow speed U and vice versa. For the case of the sech^2 profile,

$dq_0/dy=2+\beta$ at $y=0$ and so a large gradient implies a large value of β (i.e., β close to the marginal stability value of $\frac{2}{3}$). Thus according to Eq. (15) mode one is far from the central barrier.

The above considerations are kinematical in the sense that the streamfunction, and hence the potential vorticity, have been assumed and are at-best solutions to only linear order. The next question one should address is, what is the dynamical mechanism by which potential vorticity is homogenized in regions of the fluid. In essence this is the study of mixing and transport of vorticity, a complicated problem since potential vorticity is *not* a passive scalar but, in a sense, provides its own stirring. Nevertheless, it is interesting that even though potential vorticity is not passively advected, there are cases where it mixes as if it were.[21]

D. Area preserving maps

The use of Poincaré sections is by now a well-established and useful tool for studying chaos. However, if the differential equations are integrated directly, the number of points in such a plot can only be increased at the considerable cost of integration time, t. For example, to have N points $t=NT$, where T is the period of the perturbation. For statistical studies of particle motion (and hence transport), many orbits must be integrated for large values of t. For such studies it has proven advantageous to study, in lieu of the original Hamiltonian differential equations, an area preserving map. The simplest way to obtain this kind of map is to discretize the equations subject to the condition of area preservation. In fact, the construction of the map for the integrable case, where there is shear flow but no wave contribution, is exact and straightforward:

$$x_{n+1}=x_n-\delta\frac{\partial H_0}{\partial y}(y_{n+1}), \tag{39}$$

$$y_{n+1}=y_n. \tag{40}$$

Here the constant δ is related to the discretization of time. To include the effect of the waves this "zonal flow map" is perturbed as follows:

$$x_{n+1}=x_n-\delta\frac{\partial H_0}{\partial y}(y_{n+1})+f(x_n,y_{n+1}), \tag{41}$$

$$y_{n+1}=y_n+g(x_n,y_{n+1}); \tag{42}$$

to be area preserving,[9]

$$\frac{\partial f}{\partial x_n}+\frac{\partial g}{\partial y_{n+1}}=0. \tag{43}$$

The explicit form of the functions f and g is determined by the equations of motion. When only a single mode is present, the equation of motion for the y coordinate in a frame comoving with the mode is given by

$$\frac{dy}{dt}=-\varepsilon k\phi(y)\sin kx. \tag{44}$$

Discretization of this equation gives

$$g=-\varepsilon\delta k\phi(y_{n+1})\sin kx_n, \tag{45}$$

while the function f can be obtained from the area preservation condition. Thus the following map is obtained:

$$x_{n+1}=x_n-\delta\frac{\partial H_0}{\partial y}(y_{n+1})-\varepsilon\delta\frac{d\phi}{dy}(y_{n+1})\cos kx_n, \tag{46}$$

$$y_{n+1}=y_n-\varepsilon\delta k\phi(y_{n+1})\sin kx_n. \tag{47}$$

This map is complicated by its implicit form; from the initial points x_n and y_n one first obtains y_{n+1} by solving Eq. (47) by, e.g., Newton's method, then with this value, x_{n+1} is obtained from Eq. (46). However, an explicit map can be obtained by expanding the functions H_0 and ϕ near $y=0$,

$$x_{n+1}=x_n+a(1-y_{n+1}^2), \tag{48}$$

$$y_{n+1}=y_n-b\sin x_n, \tag{49}$$

where the variables x, y have been scaled by k and $\sqrt{|u''(0)|/2}$, respectively, and the parameters a and b are given by

$$a=\delta k, \quad b=\varepsilon\delta k\phi(0)\sqrt{|u''(0)|/2}. \tag{50}$$

Because this map violates the twist condition,[3] that is $\partial x_{n+1}/\partial y_{n+1}=0$ at $y=0$, we call this map the *standard nontwist* map. The traveling wave map presented in Ref. 16 can be obtained as an special case by setting $a=b$. Also, the logistic twist map studied in Ref. 22 can be transformed into the map presented here. An advantage of writing the logistic twist map in the form of the standard nontwist map is that in the later the line where the twist condition is violated it is always located at $y=0$, whereas in the former the position of this line changes with the map parameters. In general, a map that violates the twist condition along a line can be locally approximated in such a region by the standard nontwist map.

For small values of a and b the map of (48) and (49) reproduces the phase space of Hamiltonian (22), including reconnection, as can be seen by comparing the iterations of the map presented in Fig. (3) with the typical phase space plots of the Hamiltonian as shown in Fig. 1. When the values of a and b are increased the map exhibits stochasticity (see Fig. 4) that does not occur in the single wave Hamiltonian system of (22). To understand the origin of this stochasticity, and the relationship with the chaotic behavior of the two waves Hamiltonian system of Eq. (21), observe that if x_n and y_n denote $x(t)$ and $y(t)$ just before the time $t=n$, then the discrete map of (48) and (49) can be obtained by direct integration of the following equations:

$$\frac{dx}{dt}=a(1-y^2),$$
$$\frac{dy}{dt}=-b\sin x\sum_{m=-\infty}^{\infty}\delta(t-m). \tag{51}$$

The Hamiltonian for these equations is given by

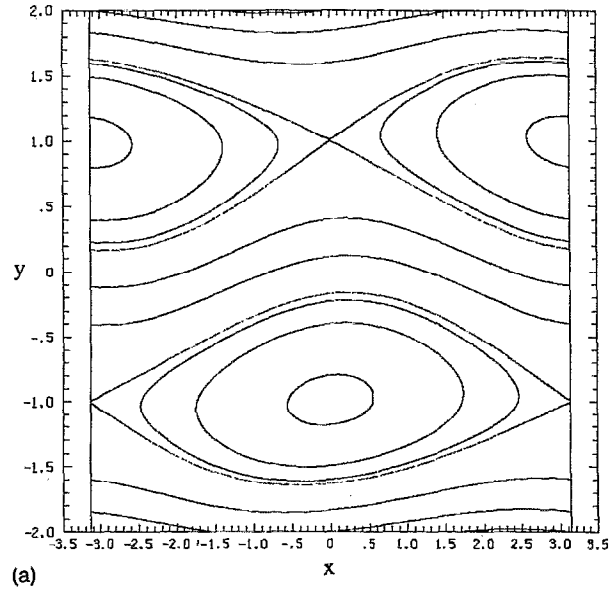

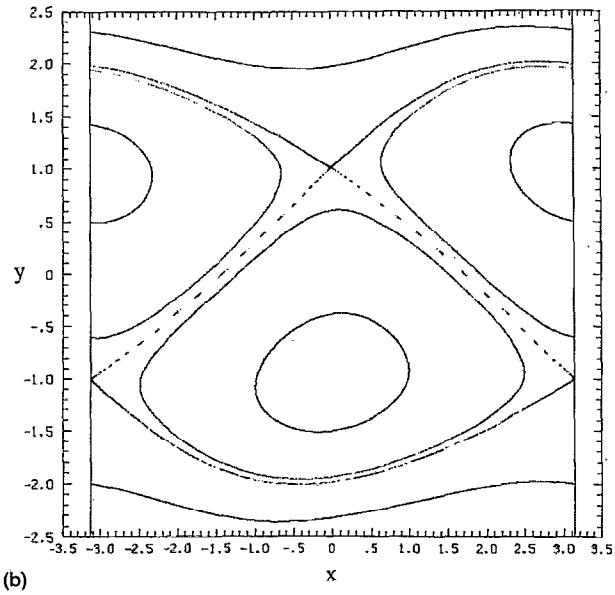

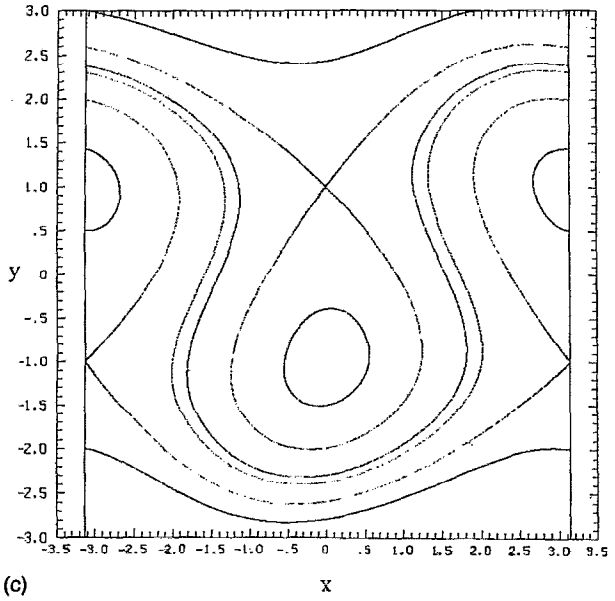

FIG. 3. Separatrix reconnection in the standard nontwist map of Eqs. (48) and (49). In case (a) $a=0.5$ and $b=0.125$ and the map exhibits a heteroclinic-type topology. Case (b) corresponds to the predicted reconnection threshold $a=0.3$ and $b=0.2$. In case (c) the values $a=0.15$ and $b=0.3$ give a homoclinic-type topology. Compare with Fig. 1.

$$H=-ay+\frac{a}{3}y^3+b\sum_{m=-\infty}^{\infty}\cos(x-2\pi mt), \tag{52}$$

where the Fourier representation of the periodic delta function has been used. From here it is seen that the effect of the discretization is to perturb the zonal flow with an infinite number of waves. Each one of these waves will create a resonance located at

$$y_m^{\pm}=\pm\sqrt{1+\frac{2\pi m}{a}}. \tag{53}$$

Note that the position of the $m=0$ resonance is always $y=\pm 1$, whereas the positions of the other resonances depend on the value of a. In accordance with the overlap criterion, the stochasticity in the map is due to the overlap of these resonances. For small values of a all the resonances with $m\geqslant 1$ are located far from the $m=0$ resonance and therefore the motion near this resonance does not exhibit chaos. This explains the high degree of integrability of the map in situations when $a,b\ll 1$ (cf. Fig. 3). When the values of a and b are increased, the resonances approach each other and chaos ensues. Although the Hamiltonian (52) contains an infinite number of resonances, the stochasticity near $y=0$ [where the map (48) and (49) is a valid model] is mostly due to the resonances closest to this region. We can say that the stochastic behavior near $y=0$ is caused by the overlap of the $m=0$ and the $m=1$ resonances. In this respect the stochasticity in the map is similar to the stochasticity of the original Hamiltonian (21), where chaotic motion arises as a result of the resonance overlap of the two modes. However, this analogy is not perfect since the $m=0$ and $m=1$ modes in the map have identical wave numbers, whereas in the Hamiltonian (21) the overlaping modes have in general different wave numbers. In Fig. 4(a) iterations of the map are plotted for $a=1.5$ and $b=0.375$. Regions of banded chaos with trapping regions are obtained; note the presence of higher-order resonances around the primary islands and in the vicinity of the central barrier. Figures 4(b) and 4(c) show reconnection of higher-order islands in the map. In (b),

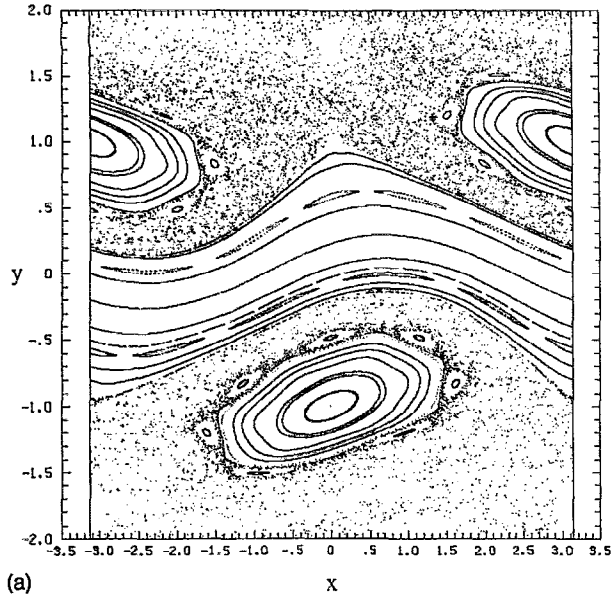

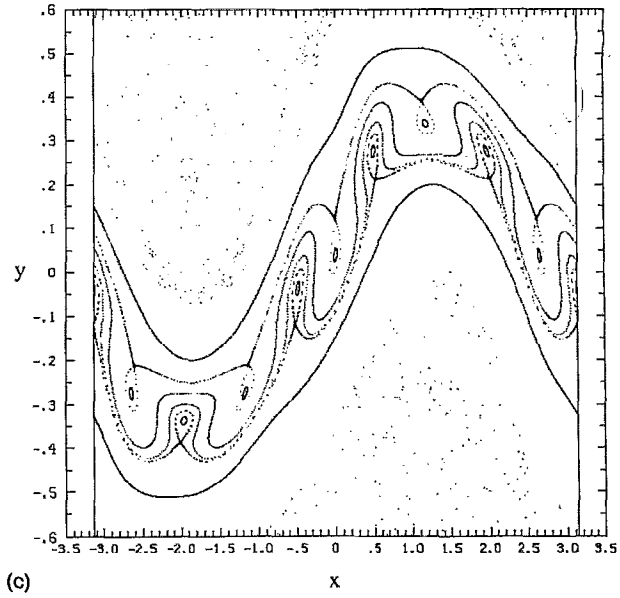

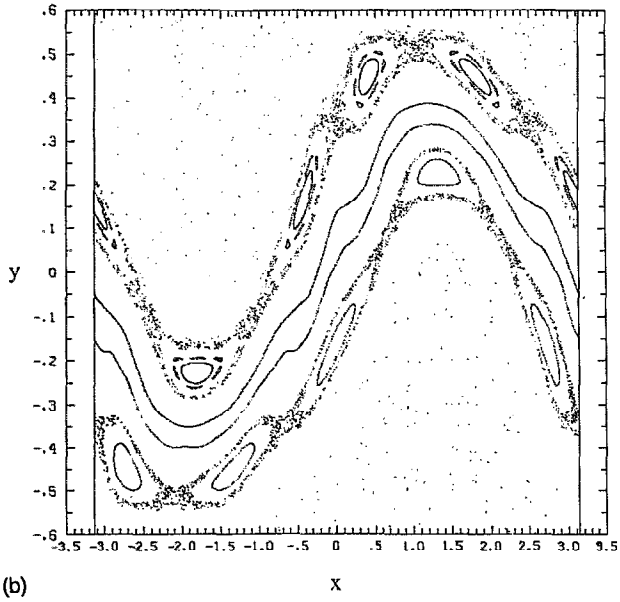

FIG. 4. Stochasticity and reconnection of higher-order resonances in the standard nontwist map of Eqs. (48) and (49). In case (a), $a=1.5$, $b=0.375$, and the map shows banded chaos with trapping regions. Note the presence of higher-order resonances around the primary islands and near the central trajectories. Cases (b) and (c) show separatrix reconnection of period five resonances. In (b) $a=2.8$, $b=0.7$ and in (c) $a=2.656$, $b=0.664$.

$a=2.8$, $b=0.7$ and in (c), $a=2.656$, $b=0.664$. As the parameters of the map vary, the period five resonances change from an heteroclinic- to an homoclinic-type structure.

The stochasticity of the map of (48) and (49) can be studied quantitatively, in the regions where the map satisfies the twist condition (i.e., $y\neq 0$), by approximating it locally by the standard map.[9] Writing $y=y_0^+ +p$, the map in neighborhood of the $m=0$ resonance, reduces to

$$\begin{aligned} x_{n+1}&=x_n-p_{n+1}\,,\\ p_{n+1}&=p_n-\kappa \sin x_n\,, \end{aligned} \tag{54}$$

which is the standard map with $\kappa=2ab$. For the standard map, the onset of widespread stochasticity occurs when κ approaches a threshold of approximately one; therefore the threshold for the $m=0$ resonances is given by $ab=\frac{1}{2}$. This result explains the high degree of integrability of the map, as observed in Fig. 3.

In the remainder of this section we derive the threshold for separatrix reconnection of primary resonances in the map. First approximate the map in the vicinity of a fixed point by a Hamiltonian system, with the Hamiltonian

$$H=-ay+\frac{a}{3}y^3+b\cos x-2\pi my. \tag{55}$$

In the system defined by Eq. (55) reconnection occurs when

$$H(x=0,y=y_0^+)=H(x=\pi,y=y_0^-).$$

After substituting Eqs. (53) and (55) into this condition, the following reconnection threshold is obtained:

$$b=\tfrac{2}{3}a. \tag{56}$$

When $b<2a/3$ the map exhibits a heteroclinic-type topology, whereas for parameter values satisfying $b>2a/3$ the map possesses an homoclinic-type topology. Figure 3

shows iterations of the map for three different values of parameters a and b. In Fig. 3(a), $a=0.5$ and $b=0.125$. Consistent with the previous results, the map exhibits the heteroclinic topology. In Fig. 3(b) the threshold values $a=0.3$ and $b=0.2$ where used. Finally, in agreement with the previous analysis, the map in Fig. 3(c), for which $a=0.15$ and $b=0.30$, has the homoclinic topology. We have numerically tested the reconnection threshold Eq. (56); for small values of a and b the reconnection process is clearly observed, as shown in Fig. 3. For large parameter values, the map exhibits widespread stochasticity and the concept of reconnection has no visible meaning. For intermediate parameter values, the stochastic layer of the primary islands is visible, and so it would be more appropriate to refer to this process as *stochastic layer reconnection.*

For a given symmetric shear flow we know u_0, and once the function ϕ is known, the map of (48) and (49) allows us to study the transport properties of the flow in the vicinity of the center of the zonal flow.

IV. CHAOTIC TRANSPORT IN THE BICKLEY JET

As an illustration of the general ideas explained above, the specific case of chaotic advection by Rossby waves in the Bickley jet is now considered. From Eqs. (18) and (21) the model Hamiltonian in this case is

$$H=-\tanh y+\varepsilon_2 \operatorname{sech}^2 y \cos k_2 x+c_2 y$$
$$+\varepsilon_1 \operatorname{sech}^2 y \cos(k_1 x-\Omega t), \tag{57}$$

where we have canonically transformed to the comoving frame of the slower wave and $\Omega \equiv k_1(c_1-c_2)$ with c_i and k_i given by Eqs. (15) and (19). The Hamiltonian for a single wave in its comoving frame is given by

$$H_i=-\tanh y+\varepsilon_i \operatorname{sech}^2 y \cos k_i x+c_i y. \tag{58}$$

Using (25) and (28) the fixed points are seen to be

$$\tilde{x}_i=\frac{n\pi}{k_i}; \quad n=0,1,..., \tag{59}$$

$$\tilde{y}_i=(-1)^n(y_i^*+\varepsilon_i), \tag{60}$$

where y_i^* is determined by Eq. (17). For $\beta=\frac{2}{3}$ the fixed points of both modes coincide at $\tilde{y}=(-1)^n[\operatorname{sech}^{-1}(1/\sqrt{3})+\varepsilon_i]$. When β tends to zero the fixed points of the fast (first) mode tend to their minimum value $\tilde{y}_1=(-1)^n[\operatorname{sech}^{-1}(\sqrt{2/3})+\varepsilon_i]$, whereas the fixed points of the slow (second) mode tend to infinity $\tilde{y}_2 \to \pm\infty$. Equation (31) implies that $(\tilde{x}_i,\tilde{y}_i)$ is stable if and only if

$$(-1)^{n+1}\tanh(\tilde{y}_i)>0. \tag{61}$$

Therefore, for n even (odd) the fixed points are shifted upward (downward) a distance ε from the critical line $[u_0(y^*)=c]$ and for n even (odd) the fixed points above $y=0$ become hyperbolic (elliptic) while those below become elliptic (hyperbolic).

As we saw in Sec. III A the separatrix reconnection threshold is obtained from the condition $H_1(P)=0$, where P denotes the hyperbolic point above the $y=0$ line. In curve (a) of Fig. 7 we have ploted the threshold as a function of ε_1 and β, as obtained from the numerical solution of the implicit equation $H_1(P)=0$. Parameter values above the curve result in an homoclinic-type phase portrait [see Fig. 1(c)], whereas parameter values below the curve give the heteroclinic type [see Fig. 1(a)]. There is a good agreement between the predicted reconnection threshold and the numerically observed thresholds [see, for example, Fig. 1(b)]. As noted before, the phase portrait will be homoclinic if the wave amplitudes are large enough and the system is far from marginality (i.e., $\beta \ll \frac{2}{3}$).

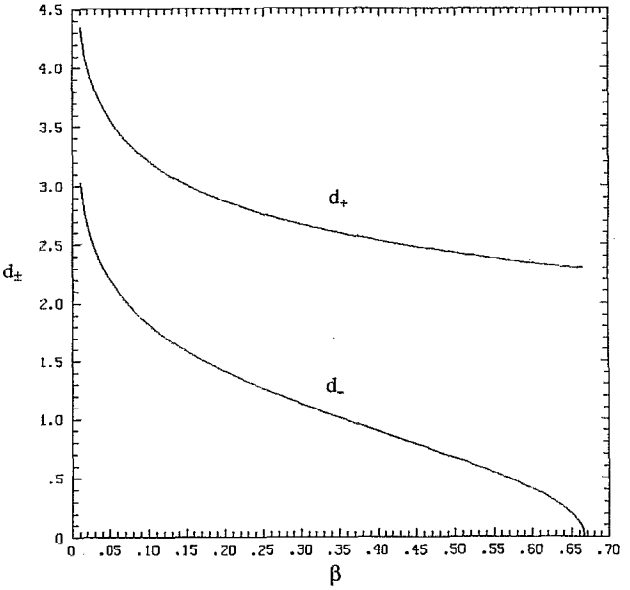

FIG. 5. Distances between the resonances as a function of beta. The distance between resonances y_2^* and $-y_1^*$ in Fig. 2 is given by d_+, while d_- gives the distance between y_2^* and y_1^*.

Now the pendulum approximation (36) is applied to the Hamiltonian of (58). Using Eqs. (37) and (17) the width of the resonances and their separation are given, respectively, by

$$W_i=\frac{2\sqrt{2\varepsilon_i}}{(1-c_i)^{1/4}} \tag{62}$$

and

$$d_\pm=|y_2^*-y_1^*|_\pm=\|\operatorname{sech}^{-1}\sqrt{c_1}|\pm|\operatorname{sech}^{-1}\sqrt{c_2}\|. \tag{63}$$

Therefore, the overlap criterion is given by the following:

$$\Lambda_\pm=\frac{\sqrt{2\varepsilon_1}}{(1-c_1)^{1/4}}+\frac{\sqrt{2\varepsilon_2}}{(1-c_2)^{1/4}}$$
$$-\|\operatorname{sech}^{-1}\sqrt{c_1}|\pm|\operatorname{sech}^{-1}\sqrt{c_2}\|=0, \tag{64}$$

where the $-(+)$ sign corresponds to banded (global) chaos. (This was previously given in Ref. 7.) Negative (positive) values of $\Lambda_\pm$ correspond to nonoverlaping (overlaping) values of β. The dependence of the width on β is weak; however, the distance between resonances depends strongly on β. Figure 5 shows the distance as a function of β. Observe that the distance d_- between the resonances on each side of the jet is small for β near $\frac{2}{3}$ and

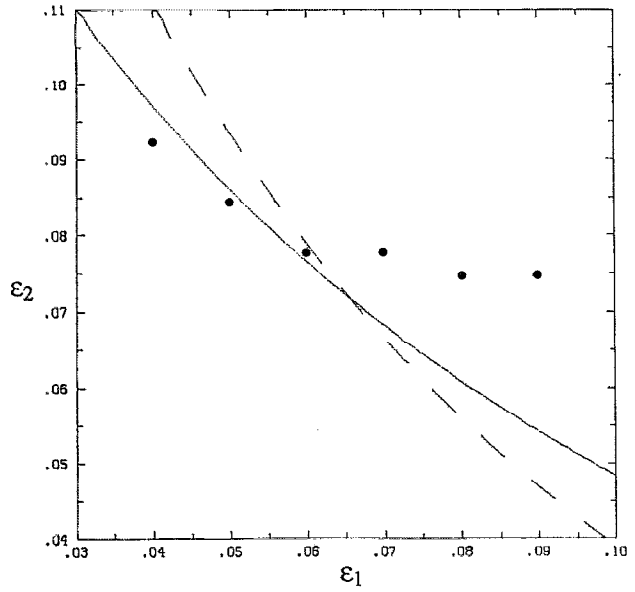

FIG. 6. Banded chaos threshold. The solid curve represents the banded chaos threshold as obtained from the resonance overlap criterion using the exact distances between the unperturbed separatrices of the primary resonances. The dashed line is the prediction obtained using the pendulum approximation. In both cases parameter values located above the curves indicates banded chaos. The dots are the numerically determined thresholds. The value of beta was set to $\beta=0.4266$.

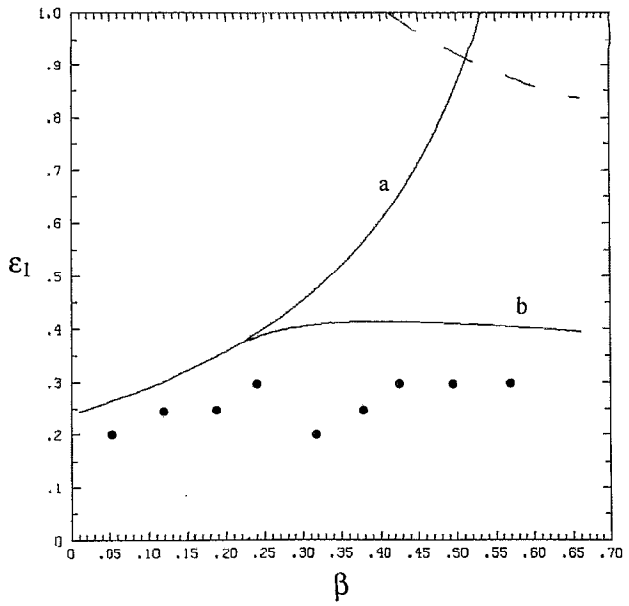

FIG. 7. Central barrier destruction threshold. Curve (a) is the reconnection threshold for mode one. Parameters values above the curve will result in a homoclinic-type phase portrait, whereas parameters below the curve will give the heteroclinic type. Curve (b) gives the threshold for resonance overlap between y_2^* and $-y_1^*$ using the exact distances between the unperturbed separatrices, while the dashed curve is the overlap in the pendulum approximation. The dots are the numerically determined thresholds. The value of ε_2 was set to $\varepsilon_2=0.3$.

so near marginality banded chaos is expected to take place for small values of epsilon.

In Fig. 6 we have plotted the resonance overlap threshold for banded chaos for $\beta=0.4266$. The dashed curve gives the threshold, as obtained by using the pendulum approximation [Eq. (64)], while the solid curve is the threshold obtained from the exact calculation of the unperturbed distance between separatrices of the resonances. The region above each curve represents values of ε_1 and ε_2 for which banded chaos is expected to exist. The dots represent an upper bound for barrier destruction obtained from numerical integration of the equations of motion for 3000 periods (one period $=2\pi/\Omega$) of the Hamiltonian. For a given value of ε_1 we increased the value of ε_2 in intervals of 0.0025 until an initial condition starting in the stochastic layer of mode one (or mode two) enters the stochastic layer of the other mode. The numerical experiments provide only an approximation to the barrier destruction threshold since the sampling of initial conditions and the maximum integration time cannot be arbitrarily large, and also because of the numerical error involved in the integration of the equations. There is good agreement between the overlap criterion and the numerical experiments for $\varepsilon_2>\varepsilon_1$. When $\varepsilon_1>\varepsilon_2$ the numerical results indicate that the last barrier to transport is more robust than what we might expect from the overlap criterion. This asymmetry between the roles of ε_1 and ε_2 is due to the asymmetric shape of the resonances (see Fig. 2). In banded chaos we consider the distance between the lower separatrix of mode two and the upper separatrix of mode one but, as Fig. 2 shows, the lower separatrix is more warped than the upper separatrix. Therefore, is easier to have overlap by increasing ε_2 (for ε_1 fixed) than by increasing ε_1 (for ε_2 fixed). The agreement between the numerical results and overlap in the pendulum approximation is not as good, since this approximation does not take into account the asymmetric shape of the resonances.

To study central barrier destruction we have plotted in curve (a) of Fig. 7 the threshold for separatrix reconnection for the Hamiltonian of Eq. (58) and in curve (b) the threshold for overlap of resonances y_2^* and $-y_1^*$ for $\varepsilon_2=0.3$, considering the exact distance between the unperturbed separatrices. The region above each curve represents values of β and ε_1 for which the central barrier is expected to be broken. The pendulum approximation, dashed curve, is not accurate in this case either because the values of ε_i are large or because the resonances are very close to the $y=0$ line. However, the analytical expression [Eq. (64)] can be used as an upper bound (albeit rather high) for central barrier destruction. The dots in Fig. 7 represent an upper bound for the central barrier destruction obtained from numerical integration of the equations of notion for 3000 periods (one period $=2\pi/\Omega$) of the Hamiltonian. The value of ε_2 was fixed at 0.3 and for each value of β we increased the value of ε_1 in intervals of 0.05 until an initial condition starting in the stochastic layer of the mode-one upper resonance y_1^* enters the stochastic layer of the mode-one lower resonance $-y_1^*$. As in the case of banded chaos above, the numerical experiments provide only an approximation to the barrier destruction threshold. As seen from the plot, the analytical estimates provide an

upper bound for central barrier destruction, consistent with the numerical results.

For small values of β the resonances of mode one are close to the $y=0$ line, and therefore the central barrier can be destroyed by separatrix reconnection for moderate values of ε_1. As β increases, the mode-one resonances separate from each other and the reconnection threshold gets bigger. At the same time the mode-two resonances become closer to the mode-one resonances, see Fig. 5, and so barrier destruction can take place, for ε_1 and ε_2 large enough, because of the overlap of resonances, as described by the Chirikov criterion.

If the system is close to marginality (β near $\frac{2}{3}$), central barrier destruction due to mode-one reconnection will occur only for very large values of ε_1. Also, near marginality the overlap of mode two and mode one will break the central barrier only if the values of ε_1 and ε_2 are large. This is because the mode-one and mode-two resonances are always separated by a finite distance, as shown in Fig. 5. Since the model is based on the assumption that the values of ε_1 and ε_2 are small, we conclude that close to marginality the central barrier persists. This is consistent with potential vorticity conservation, since at marginality there is a strong gradient of potential vorticity at the central barrier.

The above conclusions can be restated in terms of the phase velocities c_i, since these quantities determine the positions of the resonances. The closer a resonance is to the central barrier, the larger is the corresponding phase velocity. Therefore, since the dispersion relation requires the phase velocities to lie in the range $0<c_i<\frac{2}{3}$, where unity corresponds to the maximum jet velocity, the resonances can not be arbitrarily close to the center, and hence, central barrier destruction is not expected to exist. On the other hand, because at marginality the difference between the phase velocities of the two waves is small, the resonances at each side of the jet are close together, and so banded chaos is expected to occur. Below we present some numerical examples to illustrate the types of chaotic transport described.

Since the system is assumed to be periodic in the x direction the wavelength quantization condition requires $m_1\lambda_1=m_2\lambda_2=D$, where λ_i are the wavelengths, m_i the mode numbers, and D is the total length of the system in the x direction. Figure 8(a) shows a Poincaré section for the Hamiltonian (57) with $\varepsilon_1=0.1$, $\varepsilon_2=0.3$, and $\beta=0.186$, which gives, according to (15) and (19), $c_1=0.616$, $c_2=0.05$, $k_1=1.922$, and $k_2=0.548$. Here $m_1=7$ and $m_2=2$ and, accordingly, $D=22.9$. For clearer visualization only points with $x\in(0,D/2)$ were plotted. For the chosen value of β, $0>\Lambda_+=-1.55$; therefore, according to the criterion of Eq. (64) the central barrier must persist. The existence of the invariant curves in the region $y\in(-0.5,0.5)$ verify numerically this fact. On the other hand, the invariant curves starting in the neighborhood of $x=0$, $y=2.1$, and $y=-0.9$ indicate that banded chaos is also not present because these integrable trajectories separate the resonances. This fact is also in agreement with Eq. (64); since $0>\Lambda_-=-0.10$ the resonances are not close enough to destroy all of the invariant curves between them.

Figure 8(b) is a Poincaré section for the same values of ε_i, but for $\beta=0.317$. Hence, $c_1=0.575$, $c_2=0.092$, $k_1=1.857$, and $k_2=0.743$. In this case $m_1=5$ and $m_2=2$ and so $D=16.92$. Again, for simplicity, only $x\in(0,D/2)$ is shown. As in the previous case the central integrable trajectories are preserved in agreement with Eq. (64), which gives $0>\Lambda_+=-1.29$. However, in this case the resonances located above and below the line $y=0$ are close enough together, so that the invariant curves between them are destroyed, in agreement with the criterion, which gives $0<\Lambda_-=0.26$. The presence of stability islands around the primary elliptic fixed points indicate that we have banded chaos with trapping regions.

Figure 8(c) shows the extreme case of $\beta=0.614$ (same values of ε_i), $c_1=0.427$, $c_2=0.240$, $k_1=1.6$, $k_2=1.2$, $D=15.7$, $m_1=4$, and $m_2=3$. In this case $0>\Lambda_+=-0.99$ and $0<\Lambda_-=0.99$. The Poincaré section exhibits banded chaos without trapping regions and the presence of the central barrier, as expected. In this extreme case the resonances are close enough together to destroy the stability islands observed in Fig. 8(b). This fact has important consequences on the transport properties of the flow, since the islands represent regions of trapped particles.

Central barrier destruction due to reconnection of the mode-one primary resonances is shown in Fig. 8(d), for which $\varepsilon_1=0.3$, $\varepsilon_2=0.2$, and $\beta=0.119$. For large enough values of β and ε_i global chaos can be produced. Numerically global chaos is observed for $\varepsilon_1=0.5$, $\varepsilon_2=0.5$, and $\beta=0.614$.

To shed light on the consistency problem between potential vorticity conservation and chaotic transport, we have plotted in Fig. 9 the zonal flow potential vorticity,

$$q_0=2\,\mathrm{sech}^2 y\tanh y+\beta y, \tag{65}$$

for $\beta=0.614$, the same value used for Fig. 8(c). The plot reveals two regions where the potential vorticity is flat. Particles in these regions have, to first order, the same value of q_0, and thus can mix chaotically. This is indeed observed in the Poincaré section of Fig. 8(c), where bands of chaos are located above and below the central barrier at approximately the places where q_0 is constant. At the same time, the existence of the central invariant barriers is related to the sharp gradient of potential vorticity at $y=0$.

V. APPLICATION OF THE MODEL TO EXPERIMENT

In this section the model presented above is used to interpret results on transport and mixing in the rotating annulus experiments of Sommeria *et al.*[10,11] (hereafter SMS), and more recently Solomon *et al.*[24] The experiments are performed in an annular tank with a flat top and conical bottom that models the variation of the Coriolis parameter with latitude (see Fig. 10). The entire tank rotates rigidly. A corotating or "eastward" jet is generated by the action of the Coriolis force on water pumped radially inward from a set of six outlets, located on the tank bottom at a common radius, to a set of six inlets also located on the bottom but at a smaller radius. At large enough pumping rates Rossby waves are observed to propagate eastward in

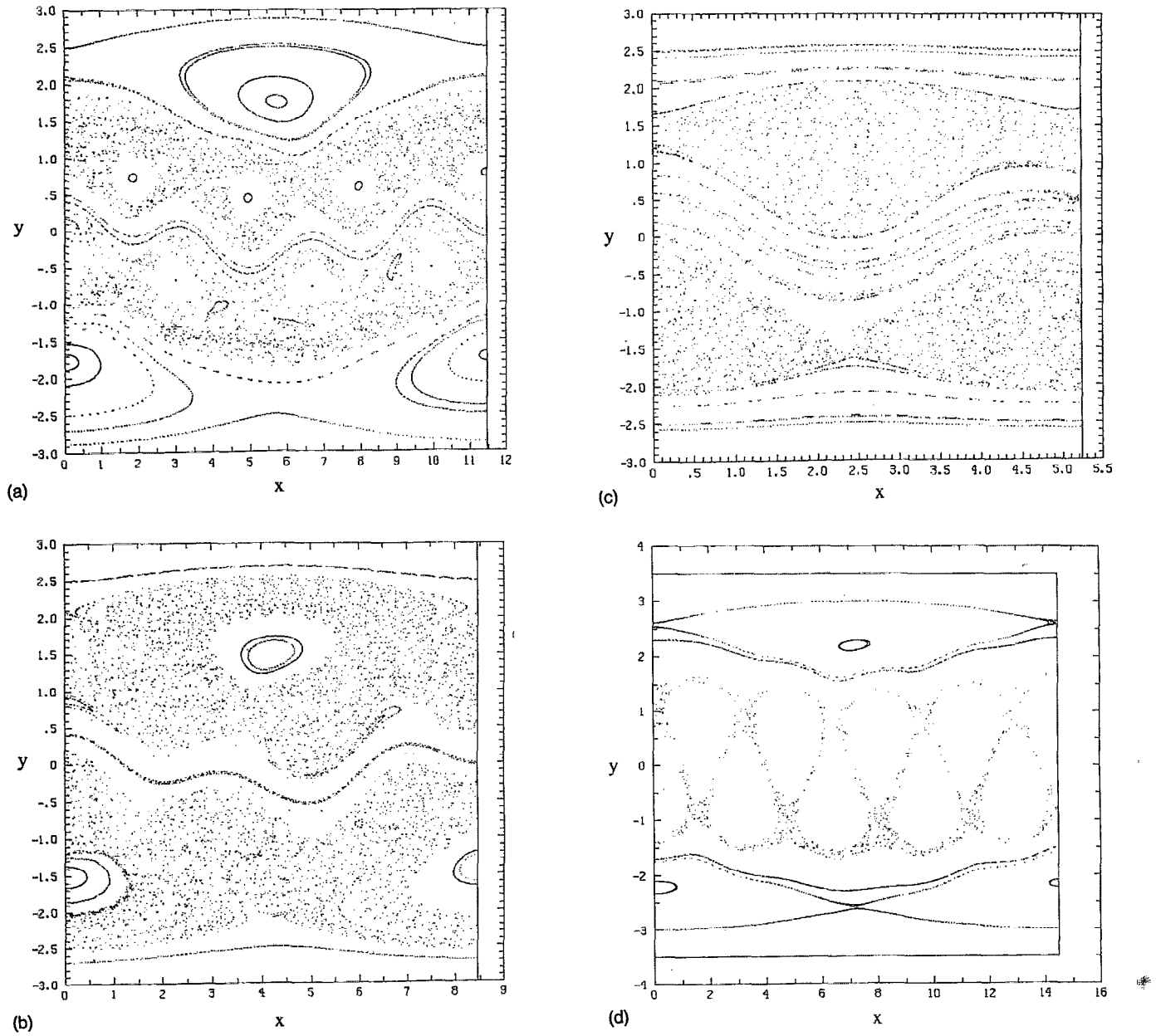

FIG. 8. Poincaré section of Hamiltonian (57) with $\varepsilon_1=0.1$, $\varepsilon_2=0.3$, and increasing values of β: (a) $\beta=0.186$, (b) $\beta=0.317$, and (c) $\beta=0.614$. The spatial periods of the system in the x direction are $D=22.9$, 16.9, and 15.7 for cases (a), (b), and (c), respectively. For a clearer visualization in (a) and (b) we only displayed points in the region $x\in(0,D/2)$ and in (c) only points with $x\in(0,D/3)$. Central barrier destruction due to reconnection and stochasticity with $\varepsilon_1=0.3$, $\varepsilon_2=0.2$, and $\beta=0.119$ is shown in (d).

the frame corotating with the tank. To elucidate the dynamics and transport SMS diagnose the experiment with particle streak photographs and dye visualization. Figure 11(a) shows an experimental contour plot of the streamfunction obtained from a particle streak photograph.[12]

Recently two models have been proposed to study the dynamics and transport observed in this experiment. Behringer *et al.*[12] proposed an *ad hoc* model of the streamfunction motivated by experimental data. Numerical integration of the equations of motion showed qualitative agreement with the experimental results. The authors of Ref. 12 observed that in their model at least three waves are needed to break the central barrier to transport. However, this conclusion is not correct, in general. In their model two waves break the central barrier, provided the appropriate values of the amplitudes and phase velocities are chosen. These values are predicted by the overlap criterion. Behringer *et al.* concentrated mostly on the wave amplitudes to study the breakup of the central barrier, but the frequencies of the waves also plays a crucial role. In Ref. 13, Polvani and Touma modeled the system using linear contour dynamics. Chaotic mixing was shown to exist on both sides of the jet when several waves are present. However, it was argued that transport across the jet can only take place through the nonlinear wave breaking of the jet itself.

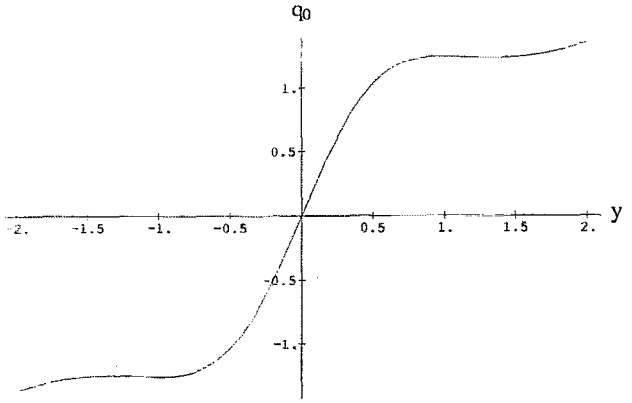

FIG. 9. Potential vorticity of the zonal flow for $\beta=0.614$, the same value used in the Poincaré section of Fig. 8(c). The potential vorticity is flat; i.e., nearly constant, in the regions where the bands of chaotic transport lie in the Poincaré section, indicating the consistent coexistence of chaotic transport and potential vorticity conservation. At the same time, the robustness of the central barrier in the Poincaré section is related to the sharp potential vorticity gradient near $y=0$.

Precise modeling of the SMS experiments is a difficult problem. These experiments were conducted at high Reynolds numbers, and therefore a precise model would require the solution of the Navier–Stokes equations with forcing. Here, however, we are more interested in the transport properties of the flow than in the exact behavior of the velocity field. Because Hamiltonian chaos exhibits generic features, transport properties of the system should not depend critically on the exact form of the streamfunction, but only upon its topology. Therefore we expect transport can be described by a simple model.

The previous sections dealt with Rossby waves propagating on shear flow in rectangular geometry, described by the Cartesian coordinates (x,y), whereas in the SMS experiments Rossby waves propagate in an annular region

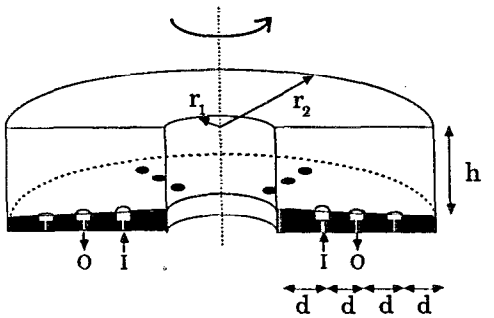

FIG. 10. Cross section of the rotating annulus used by Sommeria *et al.*[10,11] for experiments on dynamics and transport by Rossby waves. The annulus has an inner radius of 10.8 cm and an outer radius of 43.2 cm. The depth of the tank increases from 17.1 cm at the inner radius to 20.3 cm at the outer radius, resulting in a conical bottom topography with a slope equal to -0.1. The entire tank rotates at a constant angular velocity in the range from 0 to 25 rad/sec. Fluid is pumped through ports located in the bottom of the tank, the arrow indicates the pattern of inlets (I) and outlets (O). The radial distance between ports is 8.1 cm (after Sommeria *et al.*[11]).

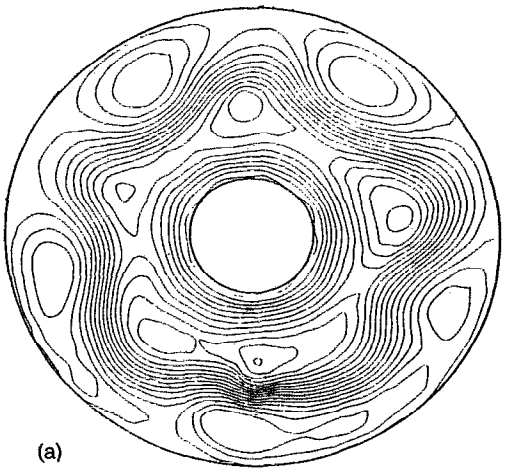

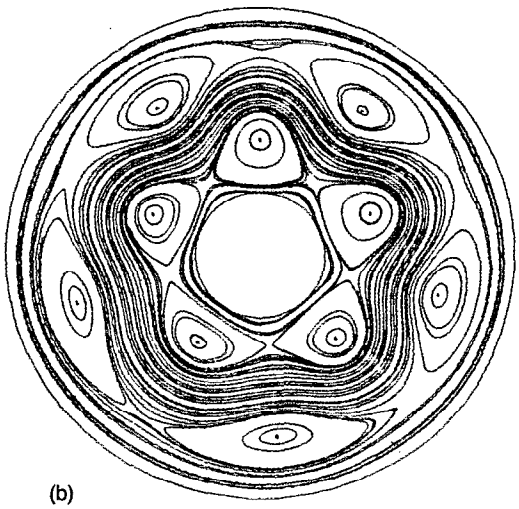

FIG. 11. (a) A Contour plot of the streamfunction deduced from a particle streak photograph of the flow (after Behringer *et al.*[12]). (b) The phase space of Hamiltonian (67) at a fixed time with parameters $A=12$ cm/sec, $r_0=25$ cm, $L=6.4$ cm, $m_1=6$, $m_2=5$, $\omega_1=1.162$ rad/sec, $\omega_2=0.632$ rad/sec, $\beta=0.64$, $\varepsilon_1=0.1$, and $\varepsilon_2=0.3$.

described by the polar coordinates (r,θ). For small jet widths and wavelengths, curvature effects of the annulus may be neglected and the results for Rossby waves propagating in the rectangular geometry can be applied to the annulus. A direct way of doing this "slab" approximation is by simply writing $y=r_0-r$ and $x=r_0\theta$, where r_0 is the radius of the maximum jet velocity. Accordingly, Eqs. (1) and (57) imply the following Hamiltonian:

$$\dot{r}=-\frac{\partial H}{\partial \theta}; \quad \dot{\theta}=\frac{\partial H}{\partial r}, \tag{66}$$

$$H=\frac{AL}{r_0}\tanh\left(\frac{r-r_0}{L}\right)+\frac{AL}{r_0}\operatorname{sech}^2\left(\frac{r-r_0}{L}\right) \times[\varepsilon_1\cos(m_1\theta-\Omega t)+\varepsilon_2\cos m_2\theta]-\left(\frac{\omega_2}{m_2}\right)r, \tag{67}$$

where

$$m_i = r_0 k_i / L, \quad \omega_i = k_i c_i (A/L),$$
$$\Omega = \frac{m_2\omega_1 - m_1\omega_2}{m_2}, \tag{68}$$

with the dimensionless k_i and c_i given by Eqs. (19) and (15).

In this model A, L, and r_0 are free parameters representing the maximum velocity, width, and mean position of the zonal flow jet. Before discussing transport, consider now some comparisons of this model with the experimentally measured velocity field. SMS observed that the azimuthal average of the azimuthal component of the velocity field fits well a sech^2 profile. The azimuthal average of v_θ of the above model in the annulus rest frame yields

$$\langle u_\theta \rangle_\theta = A \,\mathrm{sech}^2\left(\frac{r - r_0}{L}\right). \tag{69}$$

Hence, the zonal flow of the model is consistent with the experiment. Comparison of (69) with experimental results gives numerical values for the parameters A, L, and r_0. Typical values are $r_0 = 25$ cm, $L = 6.4$ cm, and $A = 12$ cm/sec. These values will be used for comparison of the model with the experiment. Another experimental fact is that the eastward jet relaxes to a state near marginal stability, that is, the width of the jet and its maximum velocity adjust so that the dimensionless beta parameter is close to the value $\frac{2}{3}$. Taking $\beta = 0.64$ yields from (68) $m_1 = 6$, $m_2 = 5$, $\omega_1 = 1.162$ rad/sec, and $\omega_2 = 0.632$ rad/sec. These values are in the range typically observed in the experiment, and will be used below. A more detailed comparison between the model and the experiment can be found in Ref. 7. In recent experiments[24] Rossby waves propagating in an eastward jet have been observed to satisfy

$$c^* = \frac{2}{3} U - \frac{\beta^*}{k^{*2}}, \tag{70}$$

where U denotes the maximum jet velocity and β^*, c^*, and k^* the *dimensional* beta coefficient, wave speed, and wave number, respectively. Equation (70) can be derived from the dispersion relation of Eqs. (15) and (19) for barotropic Rossby waves in a sech^2 flow, as presented in Sec. II. To see this first note that from Eqs. (15) and (16) $\beta = 6c_1c_2$, which with Eq. (19) gives $k_{1,2}^{*2} = \beta^*/c_{2,1}^*$. This last result in combination with the relation $c_1^* + c_2^* = \frac{2}{3}U$, obtained from Eq. (15), gives Eq. (70). Note that (70) has the same form for both modes, even though the dispersion relation of Eqs. (15) and (19) has a different form for each mode. To decide whether a mode satisfying Eq. (70) is a mode one or a mode two, we use the fact that the phase velocity of mode one (mode two) is always greater (smaller) that $U/3$. Relation (70) is *not* a dispersion relation because the set of wave speeds c^* and wave vectors k^* that satisfy it do not correspond to waves propagating in the *same* equilibrium zonal flow. The equilibrium flow depends on the width L of the sech^2 profile, and this parameter has been eliminated from the dispersion relation to get (70).

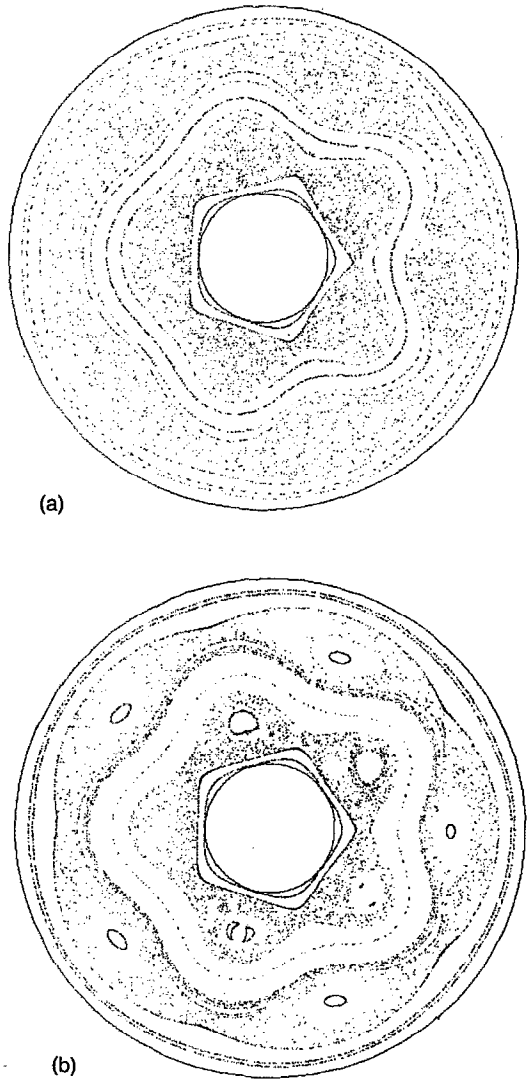

FIG. 12. Poincaré section obtained by fourth-order Runge–Kutta integration of the Hamiltonian system (67), with parameters $A = 12$ cm/sec, $r_0 = 25$ cm, $L = 6.4$ cm, $m_1 = 6$, $m_2 = 5$, $\omega_1 = 1.162$ rad/sec, $\omega_2 = 0.632$ rad/sec, $\beta = 0.64$, $\varepsilon_1 = 0.1$, and $\varepsilon_2 = 0.3$ for case (a) and $\varepsilon_1 = 0.03$ for case (b). The stability islands observed in case (b) are trapping regions.

Figure 11(b) shows a plot of the phase space portrait; i.e., contours of the Hamiltonian (67) at a fixed time, with $\varepsilon_1 = 0.1$ and $\varepsilon_2 = 0.3$. Comparison of this plot with the experimental streamfunction [Fig. 11(a)] shows reasonable qualitative agreement.

Figure 12(a) shows a Poincaré section for the model Hamiltonian of Eq. (67) for $\beta = 0.64$, $\varepsilon_1 = 0.1$, and $\varepsilon_2 = 0.3$. For these parameter values the overlap criterion gives $0 < \Lambda_- = 1.10$ for banded chaos and $0 > \Lambda_+ = -0.97$ for global chaos, which is consistent with the plot that shows the existence of banded chaos on both sides of the jet and a barrier to transport represented by the integrable wavy trajectories near the middle of the annulus. This pattern of chaotic mixing was observed in the SMS experiment when dye was injected in the outer (or inner) part of annulus.

Recent experiments conducted in the rotating annulus have shown that under certain conditions trapping regions

exist in the system. These experiments showed that dye injected in the outer part of the annulus mixes well on the injected side, except for spots or islands where dye does not enter. Particle tracking with a video camera corotating with the tank has shown that, indeed, in these regions particles are trapped. These trapping regions are imbedded in the chaotic mixing region where the particles wander freely. Figure 12(b) illustrates this situation in the model. The Poincaré section was made with the same parameters as those of Fig. 11(a), except $\varepsilon_1=0.03$. The plot shows banded chaos with trapping regions represented by the stable islands surounding the primary elliptic fixed points.

Fluid exchange across a meandering jet has been studied in Ref. 25 using the Melnikov method. The model streamfunction used in that work consists of a time-dependent perturbation of a jet of uniform width deformed by a steadily propagating sinusoidal meander. For plane wave and meander amplitude perturbations, such a streamfunction can be approximated (for small meander amplitudes) by a streamfunction of the form (21); therefore, the ideas presented in the present paper may be used to complement those obtained in Ref. 25. We mention in closing that the model streamfunction (20) and the overlap criterion (64) presented here have been used to study transport and mixing in the Gulf Stream.[26]

VI. CONCLUSIONS

We have studied transport properties of Rossby waves in symmetric shear flows. In particular, the destruction of barriers to transport was analyzed with the use of the resonance overlap criterion and the idea of separatrix reconnection. Poincaré sections were obtained numerically and compared with the analytical results.

Motivated by linear stability analysis and experimental results we proposed a Hamiltonian model to study transport in a general symmetric shear flow and, in particular, in a sech^2 zonal shear flow. We have shown that because symmetric shear flows have a maximum at $y=0$ the corresponding Hamiltonian models for these systems are degenerate ($dH_0/dy=0$ at $y=0$) and the associated area preserving maps violate the twist condition ($\partial x_{n+1}/\partial y_{n+1}=0$ at $y=0$). The general Hamiltonian can have two types of phase space portraits and the change from one type to the other is due to separatrix reconnection, a global bifurcation that exists because of the degeneracy of the Hamiltonian. We have shown how the threshold for reconnection can be obtained with the use of the Hamiltonian function.

The system exhibits two types of barriers to transport. On one hand there is the central barrier to transport formed by the integrable trajectories near $y=0$ (i.e., those between the y_1^* and the $-y_1^*$ resonances) and on the other hand there are the barriers between mode-one and mode-two resonances above and below the central trajectories (i.e., between $\pm\, y_2^*$ and $\pm\, y_1^*$). Banded chaos corresponds to the situation where the central barrier is preserved, but the barriers between the resonances above and below have been destroyed. An approximate threshold for banded chaos was obtained with the use of the resonance overlap criterion. The destruction of the central barrier was studied by considering simultaneously, the threshold for resonance overlap, as described by the Chirikov criterion and the threshold for separatrix reconnection. The connection between the gradients and regions of constant potential vorticity and the barriers to transport and mixing regions was discussed.

From the Hamiltonian model an area preserving map termed the standard nontwist map was obtained. It was shown that the map reproduces the phase space portrait, including reconnection, and the transport properties of the Hamiltonian. The role of the reconnection of higher-order resonances in the map near the central barrier was illustrated numerically.

The previous results, which are applicable in general to the description of transport by traveling waves in a symmetric flow, were then used to study transport by Rossby waves in a sech^2 zonal flow. Numerical results show that the overlap criterion gives a good estimate for the onset of banded chaos for $\varepsilon_2>\varepsilon_1$; for $\varepsilon_1>\varepsilon_2$ the numerical results indicate that the barrier is more roboust than what we expect from the resonance overlap criterion. It was shown that the analytical estimates for central barrier destruction, based on the overlap criterion and separatrix reconnection, provide an upper bound for the threshold consistent with the numerical results.

Finally, the model was used to explain results on transport and mixing in the rotating annulus experiments. Qualitative agreement was seen between the model and the experiment. Also, transport and mixing observed in the experiments appears to be well described by the model, which exhibits, in accordance with the overlap criterion, high mixing on the sides of the jet (banded chaos) and no transport across the jet.

To conclude we mention that there is a close analogy (both in the dynamics and in the transport properties) between Rossby waves and drift waves in magnetized plasmas. Drift waves are low-frequency electrostatic perturbations of nonuniform magnetized plasmas and are believed to play an important role in the magnetic confinement properties of fusion plasmas. Drift wave dynamics is governed by an equation similar to the Rossby wave quasigeostrophic equation. Analogous to the case of Rossby waves, passive advection by drift waves is described by Hamilton's equations, Eq. (1), with the plasma potential playing the role of the Hamiltonian (see Ref. 27 and references therein). Because of this, theory and experiments on Rossby waves in rotating fluids may serve as a means to simulate and study the dynamics and transport properties of drift waves. In particular, the SSM experiment and the model presented here (Rossby waves propagating in a shear flow) might shed light on drift wave transport in the presence of a sheared electric field.

ACKNOWLEDGMENTS

The authors acknowledge many fruitful conversations with W. Holloway, S. Meyers, T. Solomon, and H. Swinney, and thank them for sharing their experimental results.

DdCN acknowledges support by the Instituto de Ciencias Nucleares Universidad Nacional Autonoma de Mexico. This work was supported by the U.S. Department of Energy, Contract No. DE-FG05-80ET-53088.

[1]The sech^2 shear flow is also known as the "Bickley jet" after W. C. Bickley [Philos. Mag. **23**, 727 (1937)], who obtained this velocity profile as a solution of the boundary layer equations for a two-dimensional jet.
[2]J. Pedlosky, *Geophysical Fluid Dynamics*, 2nd ed. (Springer-Verlag, New York, 1987).
[3]R. S. MacKay and J. D. Meiss (editors), *Hamiltonian Dynamical Systems: A Reprint Selection* (Hilger, London, 1987).
[4]H. Aref, "Stirring by chaotic advection," J. Fluid Mech. **143**, 1 (1984).
[5]J. Chaiken, R. Chevray, M. Tabor, and Q. M. Tan, "Experimental study of Lagrangian turbulence in a Stokes flow," Proc. R. Soc. London Ser. A **408**, 165 (1986).
[6]J. M. Ottino, "Mixing, chaotic advection and turbulence," Annu. Rev. Fluid Mech. **22**, 207 (1990).
[7]D. del-Castillo-Negrete and P. J. Morrison, "Hamiltonian chaos and transport in quasigeostrophic flows," *Research Trends in Physics: Chaotic Dynamics and Transport in Fluids and Plasmas*, edited by I. Prigogine, W. Horton, Y. I. Ichikawa, and G. Zaslavsky (AIP, New York, 1993).
[8]B. V. Chirikov, "A universal instability of many-dimensional oscillator systems," Phys. Rep. **52**, 263 (1979).
[9]A. J. Lichtenberg and M. A. Lieberman, *Regular and Stochastic Motion* (Springer-Verlag, New York, 1983).
[10]J. Sommeria, S. D. Meyers, and H. L. Swinney, "Laboratory model of a planetary eastward jet," Nature **337**, 58 (1989).
[11]J. Sommeria, S. D. Meyers, and H. L. Swinney, "Experiments on vortices and Rossby waves in eastward and westward jets," *Nonlinear Topics in Ocean Physics*, edited by A. Osborne (North-Holland, Amsterdam, 1991).
[12]R. P. Behringer, S. D. Meyers, and H. L. Swinney, "Chaos and mixing in a geostrophic flow," Phys. Fluids A **3**, 1243 (1991).
[13]L. M. Polvani and S. Touma, "A note on recent experiments with Rossby waves on eastward jets," *Nonlinear Phenomena in Atmospheric and Oceanic Sciences*, edited by G. Carnevale and R. Pierrehumbert (Springer-Verlag, New York, 1991).
[14]H. L. Kuo, "Dynamic instability of two-dimensional nondivergent flow in a barotropic atmosphere," J. Meteorol. **6**, 105 (1949).
[15]F. B. Lipps, "The barotropic stability of the mean winds in the atmosphere," J. Fluid Mech. **12**, 397 (1962).
[16]J. B. Weiss, "Transport and mixing in traveling waves," Phys. Fluids A **3**, 1379 (1991).
[17]J. B. Weiss and E. Knobloch, "Mass transport by modulated traveling waves," Phys. Rev. A **40**, 2579 (1989).
[18]T. H. Solomon and J. P. Gollub, "Chaotic particle transport in time dependent Rayleigh–Bénard convection," Phys. Rev. A **38**, 6280 (1988).
[19]V. Rom-Kedar, A. Leonard, and S. Wiggins, "An analytical study of transport, mixing and chaos in an unsteady vortical flow," J. Fluid Mech. **214**, 347 (1990).
[20]D. F. Escande, "Stochasticity in classical Hamiltonian systems: Universal aspects," Phys. Rep. **121**, 165 (1985).
[21]R. T. Pierrehumbert, "Chaotic mixing of tracer and vorticity by modulated traveling Rossby waves," Geophys. Astrophys. Fluid Dyn. **58**, 285 (1991).
[22]J. E. Howard and S. M. Hohs, "Stochasticity and reconnection in Hamiltonian systems," Phys. Rev. A **29**, 1, 418 (1984).
[23]B. J. Hoskins, M. E. McIntyre, and A. W. Robertson, "On the use and significance of isentropic potential vorticity maps," Q. J. R. Meteorol. Soc. **111**, 877 (1985); and W. R. Young, "Baroclinic theories of the wind driven circulation," *General Circulation of the Ocean*, edited by H. D. Abarbanel and W. R. Young (Springer-Verlag, New York, 1987).
[24]T. Solomon, W. Holloway, and H. Swinney, "Shear flow instabilities and Rossby waves in barotropic flow in a rotating annulus," submitted to Phys. Fluids A.
[25]R. M. Samelson, "Fluid exchange across a meandering jet," J. Phys. Oceanogr. **22**, 431 (1992)
[26]S. D Meyers (private communication, 1992).
[27]W. Horton, "Nonlinear drift waves in magnetized plasmas, Phys. Rep. **192**, 1 (1990).